

Performance of the NGST Wavefront Control System as Tested on DCATT

David Redding, Scott Basinger, Andrew Lowman, Fang Shi
Jet Propulsion Laboratory, California Institute of Technology

Chuck Bowers, Laura Burns, Pamela Davila, Bruce Dean, Mike Fitzmaurice, John Hagopian, Claudia Leboeuf, Gary Mosier, Todd Norton, Brendon Perkins, Pete Petrone, Ladd Wheeler, Mark Wilson
Goddard Space Flight Center

Abstract

The NGST wavefront control testbed (also known as DCATT) is being used to map out the accuracy and dynamic range of the baseline NGST wavefront control system. Results to date have shown that wavefront sensing and control using focal-plane imagery and phase-retrieval processing is robust and accurate, far exceeding current requirements. Good results have also been obtained for dispersed-fringe sensing, which is used during initial telescope alignment for sensing large segment piston errors. Results agree well with model predictions.

1. Introduction

The baseline NGST wavefront control (WFC) system has 2 main functions. The first is to align and phase the segments of the primary mirror and the secondary mirror to the instruments. This "Coarse Figure Control" is performed once, at the beginning of the mission (Fig. 1). It takes millimeter-level initial wavefront errors down to the sub-micron level, limited ultimately by initial segment figure quality, as described in Ref. 1. A key part of coarse phasing is "Dispersed-Fringe Sensing," in which grism interferometry is used to detect and correct segment piston errors. Recent coarse phasing results are reported in a companion paper (Ref. 2)

The second main function, "Fine Figure Control," utilizes wavefront sensing and control techniques to fine-tune alignments and deformable-mirror settings to keep the telescope diffraction-limited. Fine figure control is performed immediately following coarse figure control, and then periodically, as needed, throughout the mission. It takes the wavefront error from a few waves (peak-to-valley) to well under a wave. It compensates both alignment and figure errors, correcting segment figure errors using a deformable quaternary mirror or deformable primary mirror segments.

The telescope figure and alignments are held stable during observations by careful suppression of disturbances. This includes isolation of vibration sources onboard the spacecraft, careful structural and thermal design to minimize sensitivity to thermal changes, and active thermal control, to assure stability and predictability of the telescope with respect to attitude changes. The goal for NGST is to provide stability for days to weeks.

The overall WFC system has been engineered using detailed computer models of the spacecraft, which simulate the function and performance of the telescope in detail. Such models require validation, which is provided in part by using the same techniques to

model and then to operate a laboratory testbed with similar functionality. The “DCATT” testbed serves this function for NGST WFC.

This paper provides a status report on the ongoing development and validation of the NGST fine phasing control. Experiments have demonstrated that the fine phasing control functions are effective. Testbed performance agrees with predictions provided by modeling. At the same time, difficulties fabricating the testbed primary mirror, testbed segment actuator problems and other challenges have prompted changes to the baseline control approach.

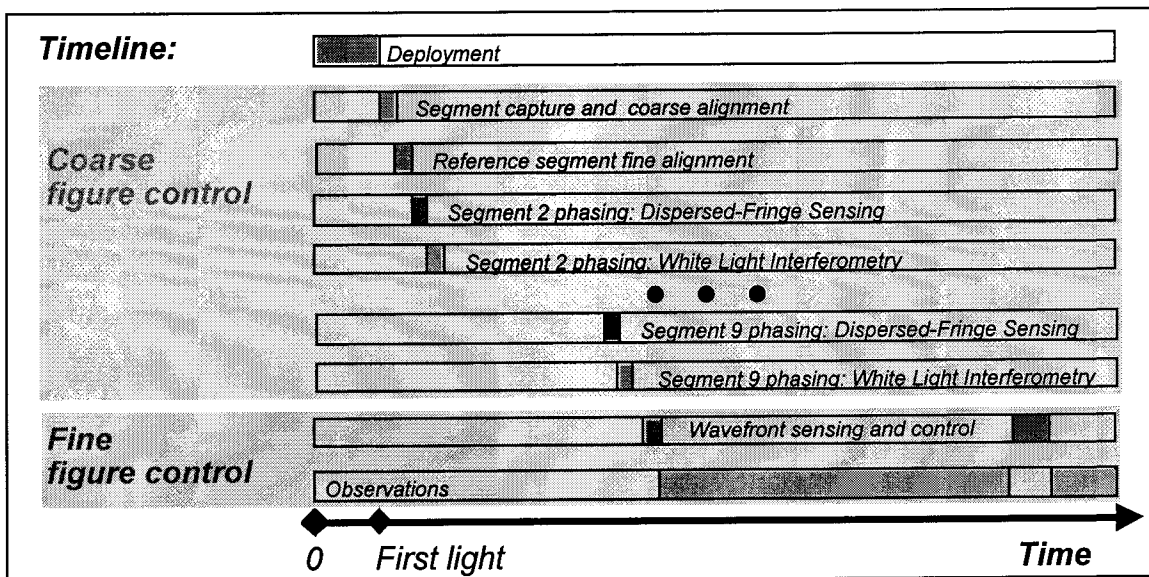


Figure 1. NGST Baseline Wavefront Control timeline.

2. Testbed Hardware

The DCATT testbed is designed as a facility for experimentation with segmented mirror telescope wavefront control. It consists of a source module, a telescope simulator module, reimaging optics including a corrector deformable mirror, and a camera. Control software provides for automation of testbed experiments, from selection of the initial aberration through implementation of the corrections and evaluation of the final PSF, making it easy to conduct Monte Carlo type experiments and develop performance statistics.

The testbed is being implemented in stages, with the first phase dedicated to proving fine-phasing control. In this configuration (the current one), the telescope simulator includes an “aberrator” deformable mirror. Later stages will add segmented optics for testing coarse figure control. A layout is shown in Fig. 2, and a detailed description is provided in Ref. 3.

A typical experiment begins by putting figure or segment alignment errors onto the simulator (DM or segmented mirror) optics. The experimenter then selects the type of function to be performed (coarse phasing, fine phasing, scoring, snapshot, etc.). Imaging parameters, such as filter wavelength, bandpass, attenuation, exposure time, and selection of dark frame subtraction and numbers of frames to be coadded are made and

implemented on the hardware. Then the experiment is run, taking pictures, processing them, moving actuators, and repeating until the experiment concludes. A more explicit example is presented in Section 4 below.

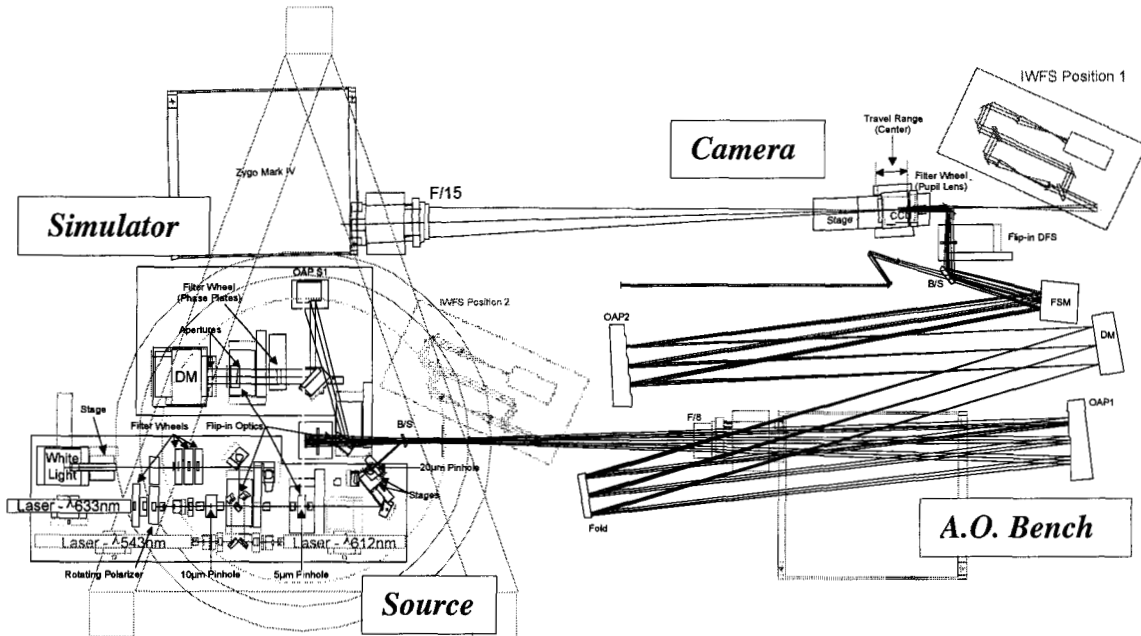


Figure 2. DCATT optical layout.

3. Wavefront Sensing and Control

Wavefront sensing and control is the final, clean-up phase of NGST figure control, taking errors from a few waves to diffraction limited. The NGST baseline WFC uses the science cameras themselves as wavefront sensors. To estimate the wavefront, several defocused images are processed, together with a pupil image, in a focus-diverse iterative-transform phase retrieval algorithm augmented with phase unwrapping. Control calculations invert the actuator-to-wavefront sensitivity matrices to generate gains; these multiply the estimated WF to compute the actuator controls.

This approach was adopted for a number of reasons:

- It does not require a dedicated instrument for wavefront sensing, avoiding considerable expense and complexity.
- It can be run in any of the NGST science cameras, at wavelengths from 600 nm to 20 um, depending on what instruments are ultimately flown. Retrievals at longer wavelengths give dynamic range of several 10's of microns; retrievals at shorter wavelengths provide better resolution. Retrievals in each camera can resolve each camera's aberrations.
- It provides an end-to-end measure of the wavefront, including all of the optics in the beam train, and adding no extraneous optics.
- It has high spatial resolution, well beyond the cutoff of the DM.

- It measures phase consistently across discontinuities in the pupil at segment boundaries, modulo 2π , unlike Shack-Hartman sensors, which are insensitive to segment piston. Estimates at 2 wavelengths can be combined to resolve piston ambiguities.
- It is operationally straightforward, requiring 4 images of an unresolved object for processing. The computer processing takes 4 minutes on a 4-processor workstation.
- Finally, as demonstrated on the WFC testbed and reported here, it is robust and accurate.

The WF sensing process begins by taking multiple images at different defocus settings. Typically images at -25 mm, -12.5 mm, 12.5 mm and 25 mm defocus are used, in a $f/16.6$ beam. A pupil image is also taken, by flipping in a pupil-imaging lens. The images are taken using a white-light source and narrow-band filters. The images are typically run to full well in the brightest pixels, about 300,000 photons for 9 μm pixels sampled with a 14-bit A-to-D converter. The images are spread over many pixels – typical images can be seen in Fig. 3.

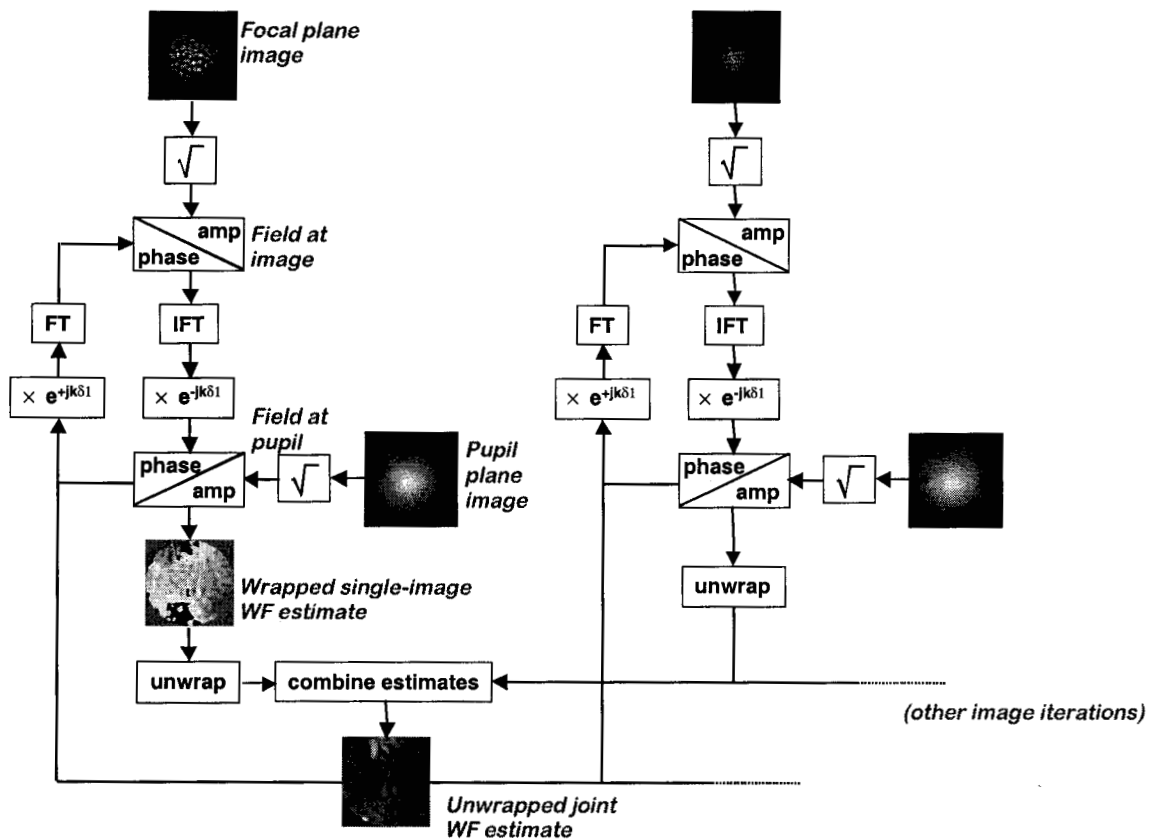


Figure 3. Focus-diverse phase retrieval algorithm.

The images are processed in a modified Gerchberg-Saxton⁴ iterative transform algorithm, sketched in Fig. 3. The inner, single-image iteration begins with a purely random guess for the phase at the exit pupil. This is combined with the square root of the pupil image to synthesize the field at the exit pupil. This field is delayed by a diversity matrix δ , which

is generated from the optical model of the system, and then propagated to the image plane. The phase of this propagated field is then combined with the square root of the image data and propagated back to the pupil plane. This iteration proceeds for 10 or so times, independently for each image. The outer, multiple-image iteration averages the phase estimates from each image, weighted by user-defined factors, to provide a common, joint estimate for phase. This is then used to restart the image iterations.

In later iterations, the image estimates are each unwrapped before combination. A simple, fast unwrapping algorithm, based on a phase-shifting and voting scheme, is employed. When unwrapping is on, the outer-loop combination process checks for and tries to resolve unwrapping artifacts across the several image iterates. Branch points and other persistent unwrapping errors do sometimes occur. These can often be resolved by numerically shifting the phase of the estimates and restarting the iteration.

With the WF estimated, the controls are readily computed using linear optimal control calculations. In its simplest form, multiplying the estimated by gain matrices produces a linear least-squares control that minimizes WF error. The gains are generated as the pseudo-inverse of the partials of wavefront error to actuator commands. The partial matrices can be measured by "poking" actuators in turn, estimating the poked phase, and subtracting the nominal phase. Partial matrices can also be computed from the models.

More complex controllers can be implemented to explicitly account for constraints in total actuator throw DM actuator-to-actuator stroke limits, and other effects. Some have suggested that the DM could be actuated modally, or in a spatial-frequency-limited mode, to limit the high spatial-frequency content of the final WF. Experience suggests, however, that DMs inherently have aberrations at their sampling resolution and beyond.

Once the controls are computed, they are sent to the testbed computers and implemented on the hardware. Then, the process is repeated. For some large initial error cases, the final correction requires 4 or 5 iterations through the entire control cycle. An example illustrates this, beginning with the introduction of aberrations using the low-resolution simulator DM, as illustrated on Fig. 4.

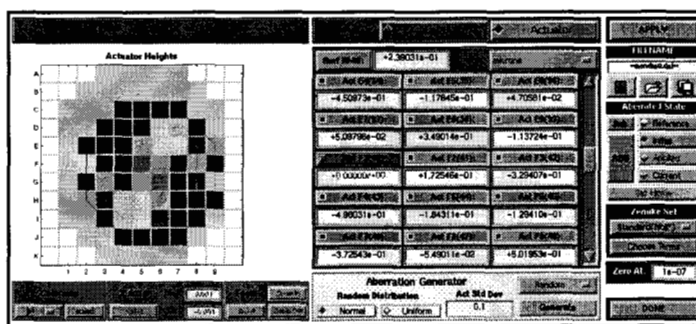


Figure 4. Simulator DM aberration control panel, showing aberrations introduced, and image that results.

Then comes a few cycles of (1) taking pictures, (2) processing the pictures using phase retrieval and phase unwrapping codes to get a phase estimate, then (3) computing new

settings for the separate, higher resolution AO DM. Three intermediate WF estimates are shown in Fig. 5. Note that the first wavefront shows residual unwrapping errors. These are identified and removed during successive iterations.

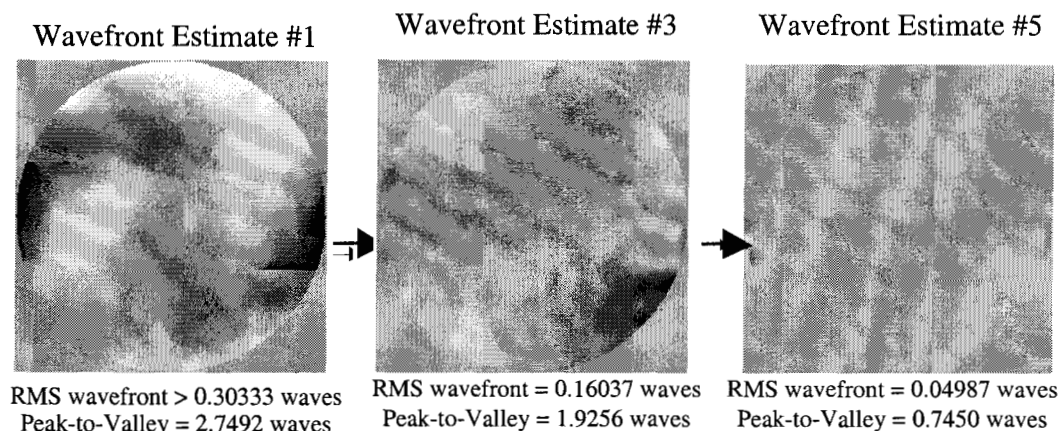


Figure 5. Wavefronts taken during correction process.

At the end of this process, the WF error is reduced from 2.7 waves peak-to-valley to about $\lambda/20$ RMS in the visible, $\lambda/60$ in the NIR. The in-focus PSF has been dramatically improved, and the AO DM correction is seen to replicate the Simulator DM (Fig. 6). The final WF does have significant high-spatial frequency residuals, as discussed later.

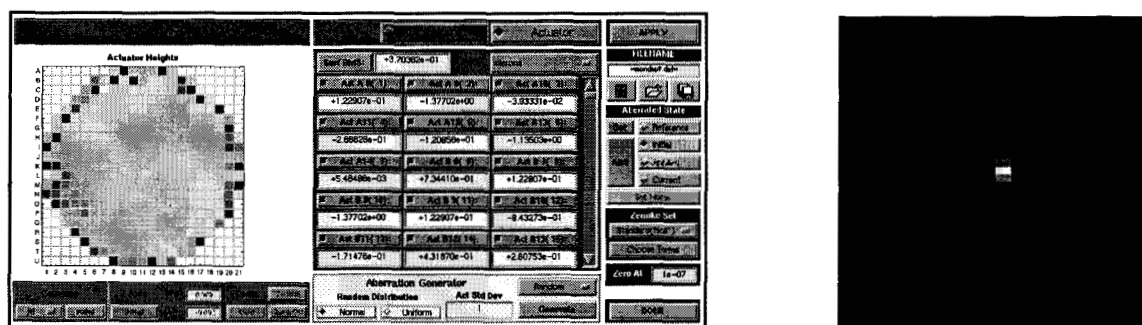


Figure 6. Final correction as seen in AO DM actuator settings, and the post-correction image.

Experiments are being conducted to determine the ultimate dynamic range and accuracy of this WF control approach. Many of these are reported in Ref. 5. Figure 7 shows a typical test of WF sensing repeatability, performed without the AO bench installed. The simulator DM was used to flatten the system. Ten WF estimates were generated of the same WF. The RMS of the averaged estimated WF, due to residual control error, was $\lambda/36$ at $\lambda = 633 \pm 1.5$ nm. The repeatability of the WF error was $\lambda/110$; the RMS standard deviation of the mean-subtracted estimates was $\lambda/240$. At our targeted NIR wavelength ($\lambda = 2$ μ m), these performance figures are: WF control residual error = $\lambda/105$; WF sensing error = $\lambda/330$. This performance is about 8 times better than is required.

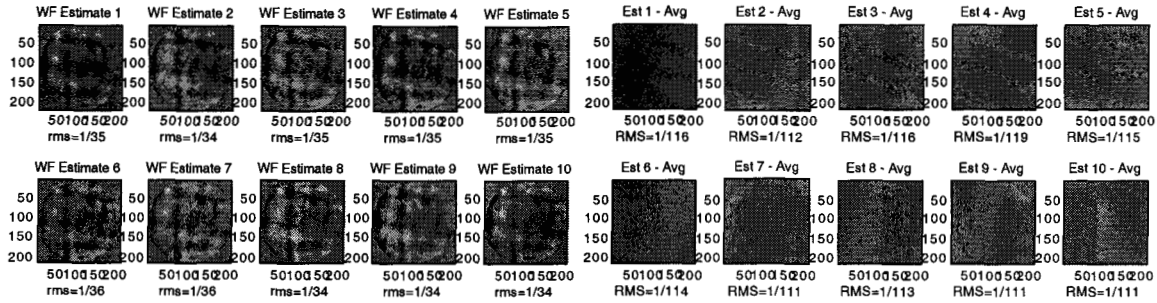


Figure 7. Ten successive measurements of the same optical system, showing estimates and deviation of estimates from the mean.

Other experiments show repeatability across wavelengths from 500-925 nm is quite consistent (Ref. 5); repeatability at successively wider spectral pass bands (3 nm to 11 or 40 nm) is also good. The phase retrieval is remarkably insensitive to jitter, at least as compared to phase-shifting interferometry. Figure 8 shows model and measured estimate error vs. jitter level, showing good performance to 2 pixels of jitter. Work continues, both in tweaking the system to get the best performance and in accumulating more definitive experimental results.

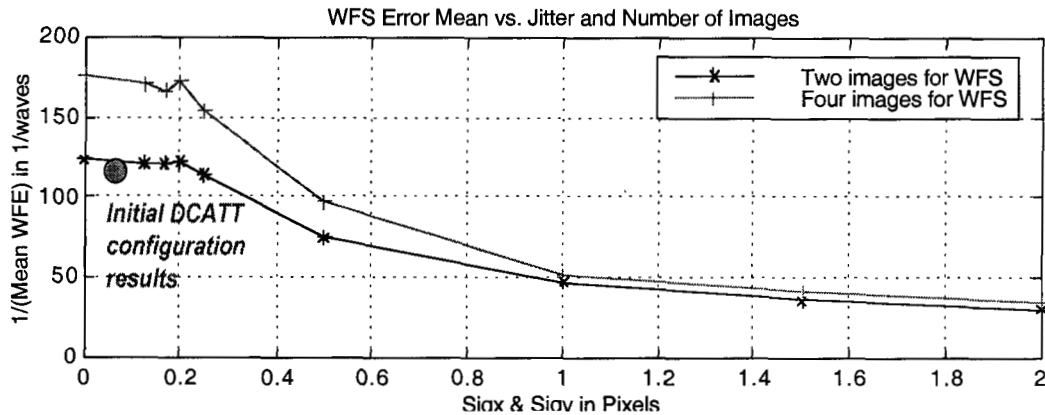


Figure 8. WF sensing error in (1/waves) at 633 nm wavelength vs. jitter in pixels.

4. Deep In-Focus Point-Spread Function

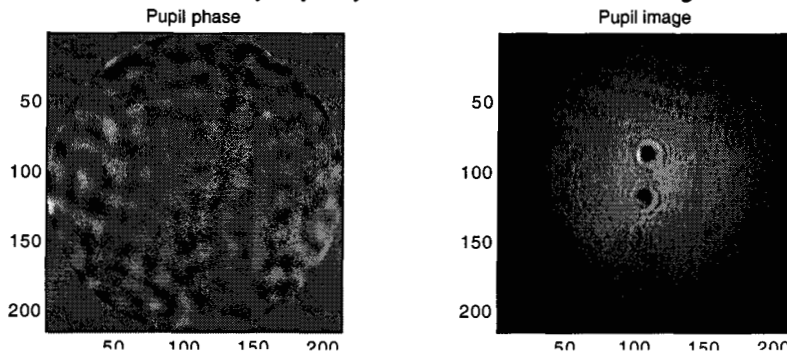
The best proof of the performance of the system – and the item the observer cares most about – is the quality of the in-focus image or PSF. This section examines a long-exposure PSF taken after flattening the WF with both the simulator DM and the AO bench DM. The data was taken at the reference focus position, very near true best focus. Approximately 80 images were taken over a period of about 1 hour and coadded to achieve a peak above 1 million counts. WF sensing was performed periodically during the exposure to monitor any changes, which were minimal. This experiment is described in detail in Ref. 6.

The resulting PSF is shown displayed on a log10 stretch as “Data” in Fig. 9. This PSF shows the expected features of a DM-corrected WF, (1) a tight core, (2) a “dark hole” with very little light surrounding the core, and (3) a squareish halo of scattered light at the

spatial frequency Nyquist limit of the DM. This limit frequency is one over twice the actuator spacing, which occurs at 10-15 pixels from the center.

This data is well predicted by model calculations based on the measured WF and pupil intensity, which are also shown on Fig. 9. The model PSF is shown as "Model" in the middle part of Fig. 9; its faint structure and core match the data well, as is best seen in the slices at the bottom of Fig. 9. Model results predicting the PSF at 2 μ m wavelength are also shown, in Fig. 10.

This measured pupil phase and intensity...



...produces these PSFs at $\lambda = 633$ nm:

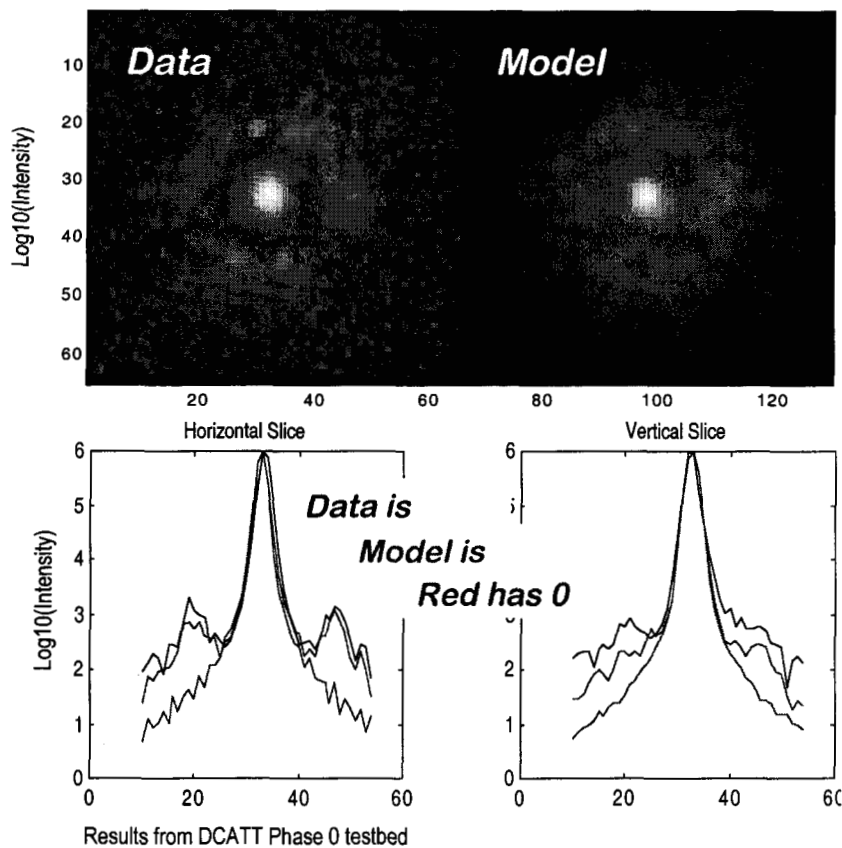
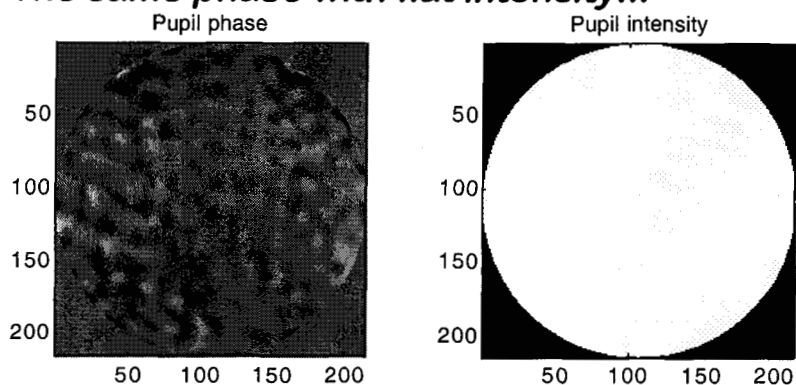


Figure 9. Deep in-focus PSF data and model.

The same phase with flat intensity...



...produces these PSFs at $\lambda = 2 \mu\text{m}$:

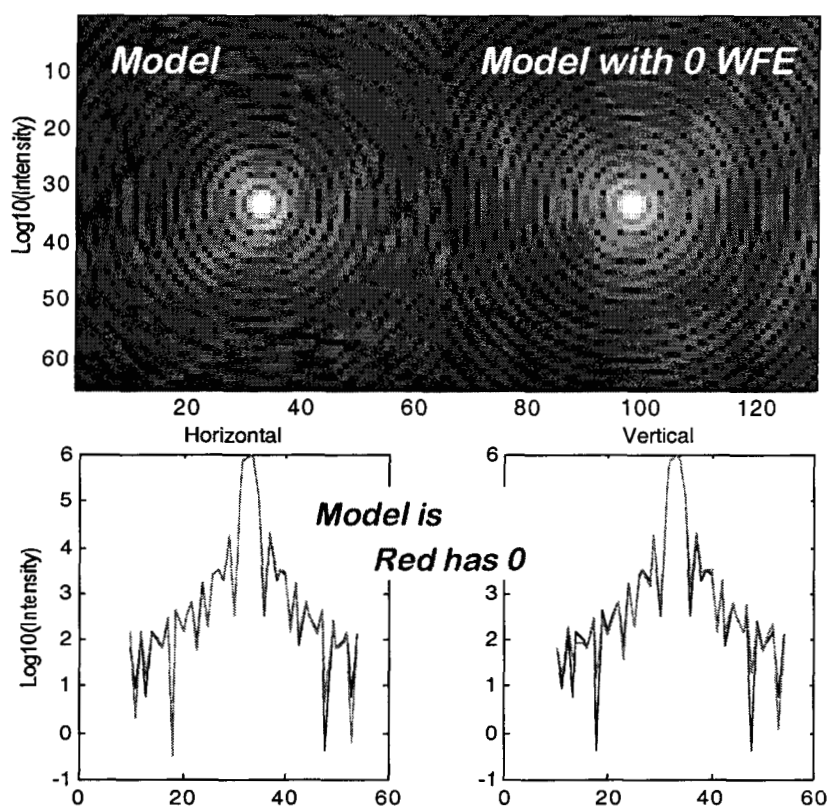


Figure 10. In-focus PSF at 2 μm wavelength.

In matching the model to the data it was discovered that the source (defined by a 20 μm pinhole convolved with a 5 μm pinhole) is resolved by the camera. This has been fixed in the hardware for future experiments. It caused blurring which is included in the model results by convolving the unblurred PSF with an appropriate Gaussian.

“Zero WFE” results are also shown in the bottom row of Fig. 9. These show slices across the PSF that would be obtained if the DM were perfect and there was no phase error in

the beam. The core matches well to this ideal PSF. The halo, which contains about 7% of the total light, disappears in the ideal PSF.

The model is also used to predict the PSF at 2 μm wavelength, as seen in Fig. 10. Here the phase is as measured -- the corrected WF phase achieved by the DCATT WF controller. The pupil illumination is assumed flat, consistent with an astronomical observation. The model shows an essentially perfect PSF, with about 1% total energy spread out in the wings of the PSF.

What are the performance limiting factors for fine phasing? Further experimentation is underway to definitively answer this question, but the main factors are clear:

- DM fitting error, set by the actuator spacing and stroke; a function of the initial aberration amplitude and spatial frequency.
- DM figure error, caused by imperfect DM polishing and coating.
- Actuation error. Segment actuation errors sets the basic noise floor. Segment errors are filtered by the DM, but imperfectly. DM actuation errors are smaller.
- WF sensing error, a function of many things, but smaller than the other errors.

5. Conclusion

Testbed experiments show that the baseline NGST fine phasing system performs better than is required, by a healthy margin. Testing also shows excellent performance for the dispersed-fringe sensor, used in initial phasing of the segments, as discussed in Ref. 2.

6. Acknowledgement

This work was performed at the Jet Propulsion Laboratory, California Institute of Technology, under contract with NASA.

7. References

1. D. Redding, S. Basinger, A. Lowman, F. Shi, P. Bely, R. Burg, G. Mosier, "Wavefront Sensing and Control for a Next Generation Space Telescope," SPIE 3356-47, http://ngst.gsfc.nasa.gov/public/unconfigured/doc_440_1/ngstWFC.pdf
2. F. Shi, D. Redding, A. Lowman, S. Basinger, C. Bowers, P. Davila, M. Wilson, T. Norton, R. Boucarout, P. Petrone, "DCATT Dispersed Fringe Sensor: Modeling and Experimenting with Transmissive Phase Plates," NGST Science and Technology Symposium, Hyannis MA, Sept. 1999.
3. C. Leboeuf, P. Davila, D. Redding, A. Morell, A. Lowman, M. Wilson, E. Young, L. Pacini, D. Coulter, "Developmental cryogenic active telescope testbed, a wavefront sensing and control testbed for the next generation space telescope," <http://dcatt.gsfc.nasa.gov/documents/papers/3356-72.pdf>
4. R.W. Gerchberg and W.O. Saxton, "A Practical Algorithm for the Determination of Phase from Image and Diffraction Plane Pictures," Optik 35, 237-246 (1972).
5. David Redding, Scott Basinger, Andrew E. Lowman, "DCATT Source, Simulator and Wavefront Sensor Camera Preliminary Performance Assessment," <http://dcatt.gsfc.nasa.gov/hottopics/ht-assessment.pdf>
6. C. Bowers, D. Redding, S. Basinger, L. Burns, D. Lindler, T. Norton, "DCATT Deep PSF Test," NGST internal report, Nov. 1999, <http://dcatt.gsfc.nasa.gov/documents/opti/anls/OPTI-ANLS-002.pdf>